

Article

Automated Extraction of Surface Water Extent from Sentinel-1 Data

Wenli Huang ^{1,*} , Ben DeVries ¹ , Chengquan Huang ¹, Megan W. Lang ^{1,2}, John W. Jones ³ , Irena F. Creed ⁴  and Mark L. Carroll ^{5,6}

¹ Department of Geographical Sciences, University of Maryland, College Park, MD 20742, USA; bdv@umd.edu (B.D.); cqhuang@umd.edu (C.H.)

² U.S. Fish and Wildlife Service, National Wetlands Inventory, Falls Church, VA 22041, USA; megan_lang@fws.gov

³ U.S. Geological Survey, Eastern Geographic Science Center, Reston, VA 20192, USA; jwjones@usgs.gov

⁴ School of Environment and Sustainability, University of Saskatchewan, 323 Kirk Hall, 117 Science Place, Saskatoon, SK S7N 5C8, Canada; icreed@uwo.ca

⁵ Biospheric Sciences Laboratory, NASA Goddard Space Flight Center, Greenbelt, MD 20771, USA; mark.carroll@nasa.gov

⁶ Science Systems and Applications Inc., Lanham, MD 20706, USA

* Correspondence: wlhuang@umd.edu; Tel.: +1-301-314-0220

Received: 6 March 2018; Accepted: 17 May 2018; Published: 21 May 2018



Abstract: Accurately quantifying surface water extent in wetlands is critical to understanding their role in ecosystem processes. However, current regional- to global-scale surface water products lack the spatial or temporal resolution necessary to characterize heterogeneous or variable wetlands. Here, we proposed a fully automatic classification tree approach to classify surface water extent using Sentinel-1 synthetic aperture radar (SAR) data and training datasets derived from prior class masks. Prior classes of water and non-water were generated from the Shuttle Radar Topography Mission (SRTM) water body dataset (SWBD) or composited dynamic surface water extent (cDSWE) class probabilities. Classification maps of water and non-water were derived over two distinct wetlandscapes: the Delmarva Peninsula and the Prairie Pothole Region. Overall classification accuracy ranged from 79% to 93% when compared to high-resolution images in the Prairie Pothole Region site. Using cDSWE class probabilities reduced omission errors among water bodies by 10% and commission errors among non-water class by 4% when compared with results generated by using the SWBD water mask. These findings indicate that including prior water masks that reflect the dynamics in surface water extent (i.e., cDSWE) is important for the accurate mapping of water bodies using SAR data.

Keywords: wetlands; surface water extent; inundation; Sentinel-1; synthetic aperture radar (SAR)

1. Introduction

Wetlands are among the world's most productive and ecologically diverse ecosystems; yet, they are being lost at alarming rates [1,2]. Accurately quantifying the spatial and temporal dynamics of surface water in wetlands is critical to understanding ecosystem processes, including land-atmosphere energy balance [3], carbon and nutrient cycles [4,5], wetland modeling [6] and surface-groundwater dynamics [7,8]. Despite this critical need, most regional- to global-scale surface water extent products do not adequately characterize spatially complex or temporally dynamic wetlands due to their limited spectral, spatial or temporal resolutions [9,10].

A limitation of products derived from optical sensors stems from their inability to penetrate cloud cover, which often coincides with flood events. Products derived from optical sensors such as

Landsat [11] and Sentinel-2 [12] normally use a variety of spectral bands ranging from visible to the shortwave infrared (SWIR) regions of the electromagnetic spectrum.

Active sensors, such as synthetic aperture radars (SAR), have advantages over optical sensors to quantify the spatial and temporal variation of surface water extent [13]. These advantages include ‘all-weather’ and ‘day-and-night’ capacity, as well as sensitivity to both open water and below-canopy inundation [14–19]. Detection of surface water using SAR backscatter relies on the fact that areas of open, smooth (no or small waves relative to the wavelength of energy employed by the SAR) water bodies typically exhibit lower backscatter coefficients [14]. SAR backscatter coefficients from both spaceborne and airborne platforms have been employed for mapping surface water extent in emergent flood events and a variety of ecosystems, including lakes, rivers, and wetlands [16,19,20]. Many SAR-based studies employed either histogram thresholding methods [16,21,22], classification approaches [14,23] or multi-temporal thresholding [24] to map water surface extent. A number of studies have explored the influence of incidence angle [22,25,26], wave conditions [21,27], and vegetation cover [15,17] on SAR backscatter. Numerous operational mapping algorithms rely on SAR backscatter from single-polarized (e.g., HH, HV, or VV), dual-polarized (HH/HV or VV/VH) [28–30], or quad-polarized (HH/HV/VV/VH) data [23,31], where the first and second letter denote transmit and receive polarizations.

Despite these advantages, there are few SAR-based sub-hectare (100 m) surface extent products at continental to global scales. The main reason these products have not been developed is the limited availability of SAR data [16], which results in spatial and temporal discontinuities when quantifying the dynamics of surface water extents across broader geographic regions. Until recently, systematically collected SAR datasets, such as that from the Sentinel-1 satellite, have not been available. The European Space Agency currently provides publicly available Sentinel-1 SAR data with potentially global coverage that may greatly improve land surface monitoring [32].

Automated algorithms are essential for surface water mapping at large geographic scales [18,22,33]. Traditionally, the selection of a training dataset is one of the tedious and subjective steps that impede the automation in either thresholding or classification algorithms. Recently, several studies demonstrated the feasibility of automatically selecting training datasets from existing data products to generate newer and enhanced products [34–36]. Among these products, the Shuttle Radar Topography Mission (SRTM)-derived water body dataset (SWBD) is one of the more commonly used datasets, perhaps in part because it has a relatively fine spatial resolution (90 m) compared to other products with near global coverage [37]. Such products include open permanent water bodies (SAR-WBI) derived from the Envisat advanced synthetic aperture radar (ASAR) instrument [16], and the Moderate Resolution Imaging Spectroradiometer (MODIS) water mask 250 m (MOD44W) data product [37]. In addition, global-scale data and cloud computing are now available for large-scale applications. For example, multi-temporal Landsat data were used recently to generate a global inundation surface water extent product [38], using Google Earth Engine (GEE), a platform that stores multiple sources of global-scale satellite imagery and provides planetary-scale analysis capabilities for non-profit scientists and researchers [39].

In this paper, we describe a fully-automated approach for mapping surface water extent using satellite-based Sentinel-1 C-band SAR data. A critical step in the automatic algorithm is the selection of training samples from prior masks generated by existing data products. While existing water masks can be used to automatically train a surface water classification algorithm [22], most static water masks omit small and dynamic wetlands, generating a bias in these classification models. The objective of this study was to determine the importance of including information on surface water dynamics when selecting training data for surface water classification models. Specifically, the surface water extent was mapped using a random forest approach, using water masks from either the SWBD or composites of dynamic surface water extent (DSWE) products (USGS, 2017). This paper is organized as follows. First, the representative study sites and data used for analysis are described, followed by a brief description of the prior masks prepared using SWBD and DSWE datasets. Then, the proposed

automated algorithms to classify water and non-water are described and applied to Sentinel-1 data, and accuracy assessments are performed using high-resolution images. Finally, the significance and limitations of the result are discussed and conclusions are drawn.

2. Methodology

2.1. Study Area

Two sites in North America were selected for this study, including a portion of the Prairie Pothole Region located in North Dakota and a site in the Delmarva Peninsula portion of Maryland, representing inland and coastal wetlandscapes, respectively (Figure 1). The Prairie Pothole Region (PPR) of central North America is dominated by natural grasslands with a relatively high density of small and elliptical open water bodies. The Delmarva Peninsula (DMV) is between the Chesapeake Bay and Atlantic Ocean in the eastern United States and mainly consists of cropland and forest, including many small rivers, streams, swamps in forests and marshes along the Peninsula's edge [40,41]. Both wetlandscapes contain geographically isolated wetlands (wetlands surrounded by uplands) and have a relatively flat topography.

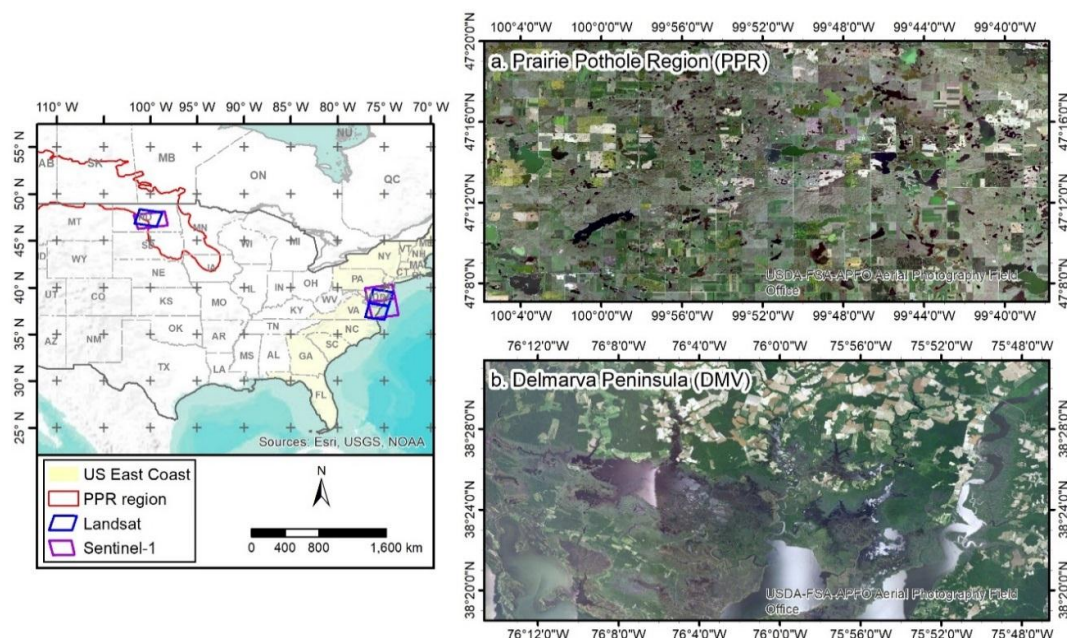


Figure 1. Map of the study sites, including the Prairie Pothole Region (PPR) and the Delmarva Peninsula (DMV), with Landsat path/row (purple solid line) and Sentinel-1 path/frame (blue solid line). National Agriculture Imagery Program (NAIP) images (right column) are given for each site, representing inland (**upper right**) and coastal (**bottom right**) wetlandscapes.

2.2. Remote-Sensing Datasets

Sentinel-1 SAR and Landsat optical data were used for algorithm development. Sentinel-1 carries a 5.405 GHz C-band imager, operating over land in three modes with various observation strategies, swath widths, and spatial resolutions [42]. With a swath width of 250-km at fine spatial resolution (5 m × 20 m), the interferometric wide-swath mode (IW) is the main operational mode over land and has the potential to benefit a diverse array of land cover studies. Two Sentinel-1 satellites, Sentinel-1A launched in September 2014 and Sentinel-1B launched in April 2016, jointly provide a nominal 6-day repeat cycle over the equator, 6-day repeat cycle over Europe, and 12-day repeat cycle over North America, allowing for continuous monitoring of surface water extent [42]. The National Aeronautics and Space Administration Alaska Satellite Facility (NASA/ASF) houses a complete archive

of Sentinel-1 SAR data processed by the European Space Agency (ESA). Dual-polarized (VV/VH) Sentinel-1 SAR data acquired under interferometric wide-swath (IW) mode processed to Level-1 ground range detected (GRD) were automatically downloaded via the ASF application programming interface (API) [43].

Two datasets were prepared for calibration of the random forest models. First, the SRTM water body dataset (SWBD) is comprised of worldwide water body outlines in a vector format generated by the National Geospatial-Intelligence Agency (NGA) and published by NASA in 2003 [44]. SWBD represents water body status as of February 2000 surveyed by the SRTM. The SWBD data is distributed in $1^\circ \times 1^\circ$ tiles, covering the land surface on Earth between 56° southern latitude and 60° northern latitude. Second, a composited dynamic surface water extent (cDSWE) was prepared using a multi-year composition of DSWE products [45]. The DSWE products were developed by the U.S. Geological Survey as part of a suite of Landsat science products that will initially be produced for the entire Landsat archive over the United States and its territories. The DSWE model is composed of independent tests designed to detect pixels composed not only of open water, but partial mixtures of water, vegetation and soil. Threshold-based and relying only on Landsat surface reflectance Level-2 science products and digital terrain data as inputs, DSWE may be broadly applied through space and time without need for scene-based training. DSWE has been rigorously tested over the Florida Everglades [45] and evaluated over other landscapes in North America, showing that DSWE classes provide a good overview of open water bodies and partially inundated surfaces under clear-sky conditions [46,47]. The cDSWE data was prepared by applying the DSWE algorithm to all available data from the Landsat 5 Thematic Mapper (TM) and Landsat 7 Enhanced Thematic Mapper (ETM+) acquired between 2000 and 2015, and calculating the class probabilities of land and water during this time period using Google Earth Engine [39].

Two datasets derived from optical imagery were used to validate the results from our automated algorithms. First, the DSWE algorithm was applied to Landsat-8 operational land image (OLI) data that had been acquired within 3 days of corresponding Sentinel-1 data over both sites and pre-processed to surface reflectance [45,48]. A summary of the Sentinel-1 and Landsat data used for this study is shown in Table 1, including acquisition date and weather data such as temperature and precipitation. For the PPR site, the weather data were recorded at Robinson, ND, by the North Dakota Agricultural Weather Network (NDAWN) system [49]. Second, we used high-resolution images (1 m) coincident with Sentinel-1 acquisitions and acquired through the National Agriculture Imagery Program (NAIP) 2016 campaign over the Prairie Pothole Region site.

Table 1. Summary of Sentinel-1 and Landsat-8 data acquired over two study sites (PPR, Prairie Pothole Region; DMV, Delmarva Peninsula). * Path/Frame for Sentinel-1 data is provided by Alaska Satellite Facility (ASF).

Site	Sensor	Path/Row (Frame *)	Date	Average Temperature (°C)	Precipitation (mm)			
					1 Day	3 Days	7 Days	
PPR	Sentinel-1A SAR	34/151	24 April 2016	6.0	0.0	0.0	13.0	
			6 May 2016	14.0	0.0	0.0	1.0	
			18 May 2016	13.5	0.0	0.0	0.5	
			30 May 2016	18.2	0.0	0.0	6.4	
			11 June 2016	18.7	9.7	9.7	9.7	
	Landsat-8 OLI	34/151	34/151	5 July 2016	19.9	0.0	3.0	3.0
				17 July 2016	19.9	8.9	8.9	48.6
				10 August 2016	20.4	11.4	11.4	11.9
				22 August 2016	20.3	0.0	4.1	29.0
				3 September 2016	20.7	0.0	8.9	8.9
DMV	Sentinel-1A SAR	106/119 106/126	9 July 2016	27.1	0.0	0.0	0.2	
DMV	Landsat-8 OLI	140/32 140/34	11 July 2016	25.1	0.0	0.0	0.2	

2.3. Automated Synthetic Aperture Radar (SAR) Algorithm for Water Extent Mapping

The automatic algorithm that was developed consisted of four steps: (A) pre-processing of Sentinel-1 SAR data to backscatter coefficient (Y^0); (B) prior class mask preparation either from SWBD or cDSWE products; (C) random forest classification by calibrating models using prior class information and covariates from Sentinel-1 data; and (D) accuracy assessment using co-incident NAIP images (Figure 2).

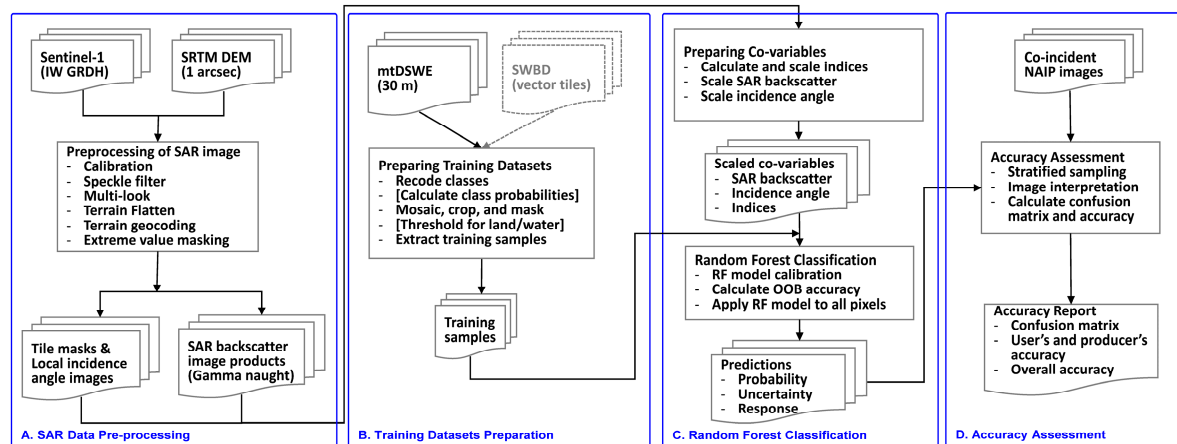


Figure 2. Workflow for mapping surface water extent using Sentinel-1 SAR data.

2.3.1. SAR Data Pre-Processing

The Science Toolbox Exploitation Platform (SNAP) Toolkit developed by ESA was used for SAR data pre-processing. Sentinel-1 intensities from high-resolution Level-1 ground range detected products (10 m; GRDH) were speckle-filtered, multi-looked, geocoded, terrain-flattened and terrain corrected to Gamma naught [50] backscatter coefficients (Y^0). Specifically, the improved Lee-Sigma filter [51] with a combination of 5×5 and 9×9 kernels were used to reduce speckle noise. The image pixels were then multi-looked (3×3 window) to 30 m square pixels and resampled using a bilinear method to match the Landsat Universal Transverse Mercator (UTM) coordinate systems. Terrain flattening and terrain correction were conducted using the recently released STRM 1 arc-second (approximately 30 m) digital elevation model (DEM) (SRTMGL1).

Sentinel-1 backscatter coefficients, band indices, and incidence angle were prepared as co-variables for classification. The Sentinel-1 intensity data available over the North American sites consisted of co-polarized VV (vertically transmitted and received) and cross-polarized VH (vertically transmitted and horizontally received) data. The local incidence angle (LIA) was included as a feature representing attributes of viewing geometry, which was found useful to differentiate water from land by previous studies [22]. Backscatter intensities were converted into decibel-scale (dB) before computing indices and carrying out the classification. A set of polarized indices were used in this study to potentially extract more information from dual-polarized radar data, and are summarized in Table 2. The polarized ratio (VHrVV) was found to separate open water from deep marsh or shallow marsh efficiently [52], and reduce systematic errors associated with acquisition systems [53]. The normalized difference polarized ratio (NDPI) was adopted from the radar forest degradation index (RFDI) reported in recent studies [54,55] to access the strength of the double-bounce signal. The NVHI and NVVI indices were adopted from the radar vegetation index (RVI), also described in literature [56,57] to reflect the level of vegetation growth.

Table 2. Polarized indices calculated from Sentinel-1 SAR data.

Index	Abbreviation	Equations	Reference
Polarized Ratio (VH to VV)	VHrVV	$Y_{VHrVV}^0 = Y_{VH}^0 / Y_{VV}^0$	Brisco et al. [52]
Normalized Difference Polarized Index	NDPI	$Y_{NDPI}^0 = (Y_{VV}^0 - Y_{VH}^0) / (Y_{VV}^0 + Y_{VH}^0)$	Mitchard et al. [54]
Normalized VH Index	NVHI	$Y_{NVHI}^0 = Y_{VH}^0 / (Y_{VV}^0 + Y_{VH}^0)$	McNairn & Brisco [56]
Normalized VV Index	NVVI	$Y_{NVVI}^0 = Y_{VV}^0 / (Y_{VV}^0 + Y_{VH}^0)$	McNairn & Brisco [56]

2.3.2. Training Datasets Preparation

Two training datasets were prepared for Sentinel-1 SAR image classification. These datasets included prior water/non-water masks derived from the SRTM water body dataset (SWBD) [44] and the composited dynamic surface water extent (cDSWE) [45]. The version 2.1 SWBD product, distributed in $1^\circ \times 1^\circ$ vector tiles, was used to build prior masks [18]. Classes of open water, including ocean, lakes and rivers, were extracted and a ‘water’ class was applied to them. The remaining pixels were included in a ‘land’ class.

As an alternative to the SWBD water mask, we used class probabilities derived from a 15-year DSWE time series to build prior masks. The data processing was completed using the Google Earth Engine, and data were exported in $1^\circ \times 1^\circ$ tiles for each site. The probability of each class was calculated as:

$$P_{\text{class}} = 100 \times N_{\text{occu}} / N_{\text{clear-sky}} \quad (1)$$

where: N_{occu} is the number of occurrences of the land, open water, and partial water DSWE classes, and $N_{\text{clear-sky}}$ is the number of clear-sky acquisitions from Landsat 5 and Landsat 7.

A threshold of 95% was applied to the cDSWE-generated probabilities to derive ‘land’, ‘water’, and ‘partial water’ masks, and the rest pixels were labeled as ‘other’. The DSWE partial surface water class was omitted from the analysis because of limited area with probability above 95%.

2.3.3. Random Forest Classification

Random forest models [58] were used to derive water classes from Sentinel-1 data. Specifically, the models described the relationship between the radar-derived covariates (i.e., radar backscattering coefficients, indices and local incidence angle) and the response variable (i.e., water/land classes from the prior masks). Samples for water/land classes were first randomly extracted using the prior masks as references. Sample sizes were proportional to the ratio of classes from the prior mask, ensuring a minimum number of 10,000 samples from the smaller of the two classes. For example, if the ratio of water to land calculated from the prior mask was 3, then we sampled 30,000 for the water class and 10,000 for the land class. For instance, a typical 30 m resolution Sentinel-1 scene in UTM projection is comprised of approximately 9498 columns and 6954 rows. An example is shown in Figure 3, which includes an image acquired on 10 August 2016 for the Prairie Pothole Region site. According to summary statistics, the number of water pixels in this image is 1,595,923, and the number of non-water pixels is 41,356,046. Therefore, we sampled 0.62% ($10,000/1,595,923$) of the water pixels and 0.48% ($200,000/41,356,046$) of non-water pixels according to the cDSWE prior mask. A random forest model with 100 trees (estimators) was then trained using the randomly sampled features as explanatory variables and water/land classes from each prior mask as response variables. A map of the probability of water class was derived by applying the trained model to all image pixels. Simple probability thresholds were selected based on recommendations from the RF model and previous studies [58,59]. Specifically, a map of water classes was derived from water probability (P_w) using rules as follows:

- If $P_w \geq 0.65$, assign a ‘high-probability water’ label
- If $0.50 \leq P_w < 0.65$, assign a ‘moderate-probability water’ label
- If $0.35 \leq P_w < 0.50$, assign a ‘low-probability water’ label
- If $P_w < 0.35$, assign a ‘non-water’ label

2.3.4. Accuracy Assessment

A visual comparison of DSWE and Sentinel-1 derived classification maps and an interpretation of the accuracy assessment of the classification results were conducted, depending on the availability of validation data over each site. For the Delmarva site, we compared the Sentinel-1 derived probability maps to DSWE maps derived from Landsat data acquired within three days of the Sentinel-1 image. Validation using NAIP imagery is not applicable for the Delmarva site because no co-incident NAIP imagery is available for the time frame of the Sentinel imagery (2015 through 2016). For the Prairie Pothole Region site, we used high-resolution NAIP images and DSWE data as reference data (Figure 3). Specifically, we randomly selected 300 points, 100 points per class, for evaluation over three classes—the persistent water, persistent land, and other mixed from Landsat derived DSWE class probabilities. Greater than 95% in either class probability (water or land) was considered as persistent in that class. Each point was visually identified from co-incident NAIP imagery acquired on the same day.

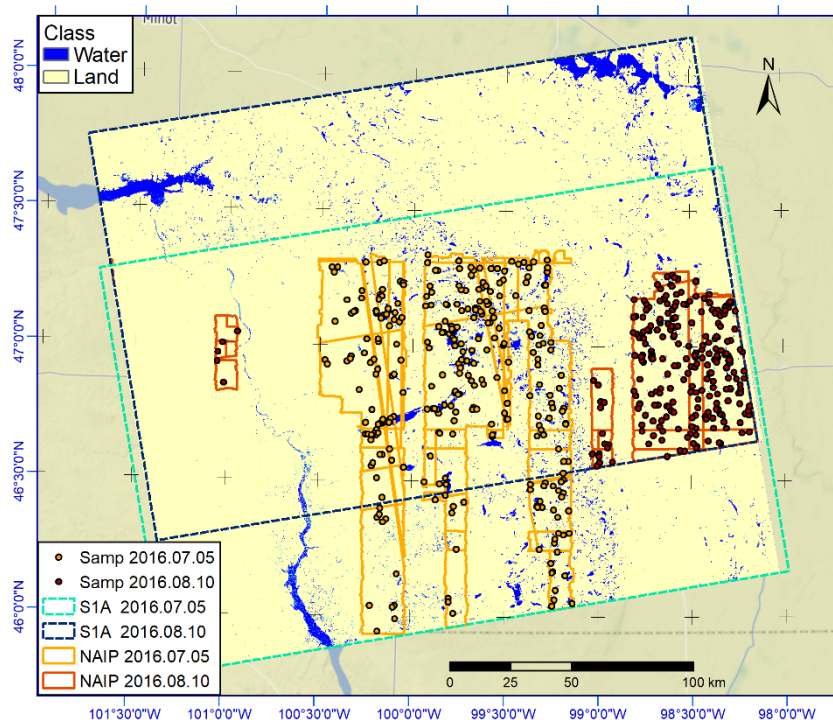


Figure 3. The Prairie Pothole Region site and footprints of remotely sensed data used in this study. The water and land class are from dynamic surface water extent (DSWE) composite class probabilities. Sentinel-1 data were collected on mid-night of 5 July 2016 (UTC) and 10 August 2016 (UTC). NAIP images were collected on the same day (noon to afternoon) of Sentinel-1 data.

2.3.5. Automation of Algorithms

Automation of the algorithms was achieved by splitting them into several fully automated sub-processes that rely on open source software and packages. First, data pre-processing was handled using the SNAP graphic processing tool (gpt), a command line interface, as embedded in bash scripts to execute in batch mode and generate a composite processing graph in Extensible Markup Language (XML). Then, several python packages ('rasterio', 'gdal' and 'numpy') were used to implement the analytical algorithms. This included the preparation of the co-variables and prior masks; the extract of training samples from the SWBD and cDSWE; random forest models model construction and execution; output the classification results; and evaluate the results.

3. Results

3.1. Comparison of Prior Masks

A comparison of the SWBD and cDSWE prior masks for the Delmarva Peninsula is presented in Figure 4. Although the general patterns were similar over major water bodies, more spatial details were preserved in the cDSWE product. Many of the pixels classified as 'land' in the SWBD mask were classified as 'partial' or 'other' in the cDSWE mask, indicating that these areas were variably classified as land or water in the DSWE time series and were thus excluded from the cDSWE mask.

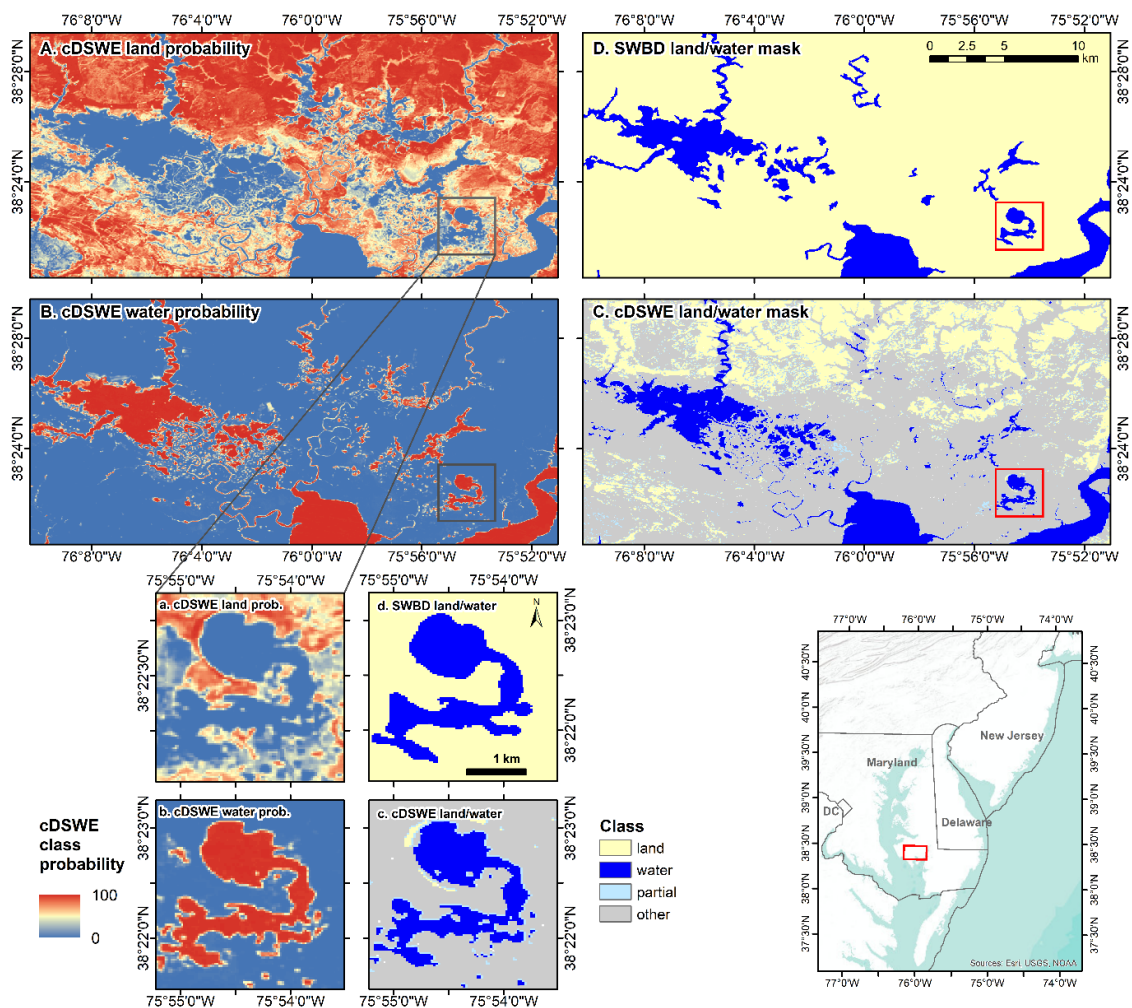


Figure 4. Land (A) and Water (B) class probabilities summarized from composited dynamic surface water extent (cDSWE) water/land classes and land/water classes derived from DSWE classes using a 95% threshold (C) and Shuttle Radar Topography Mission water body dataset (SWBD) water/land mask (D) over a site on the Delmarva Peninsula (see map). The zoom-in window (a–d) in the bottom-right shows the difference in spatial details in two products. These two prior masks were used to train and calibrate the surface water models.

3.2. Land/Water Separability from Different Radar Variables

The prior class masks described in Section 2.3.2 were used to derive training samples relating prior water/land classes to radar polarizations, indices and incidence angle. A box plot of these indices by water/land classes presented in Figure 5 demonstrates the highest class separability between water and land classes using VV and VH backscatter when compared to other indices. The separability is weak among both local and ellipsoid incidence angles and the polarized ratio index (VHrVV).

Despite the low separability compared to backscatter and polarization indices, the rationality of including incidence angle for distinguishing water from land is illustrated in Figure 6. The density scatter plot of backscatter coefficients versus local incidence angle indicated two potential classes. A plot of mean backscatter coefficients (Γ_{VV} and Γ_{VH} in dB) for each incidence angle (with $1-\sigma$ bar in grey) showed a decreasing backscatter trend with increasing incidence angle over water (in cyan), and a relative stable trend over land (in red).

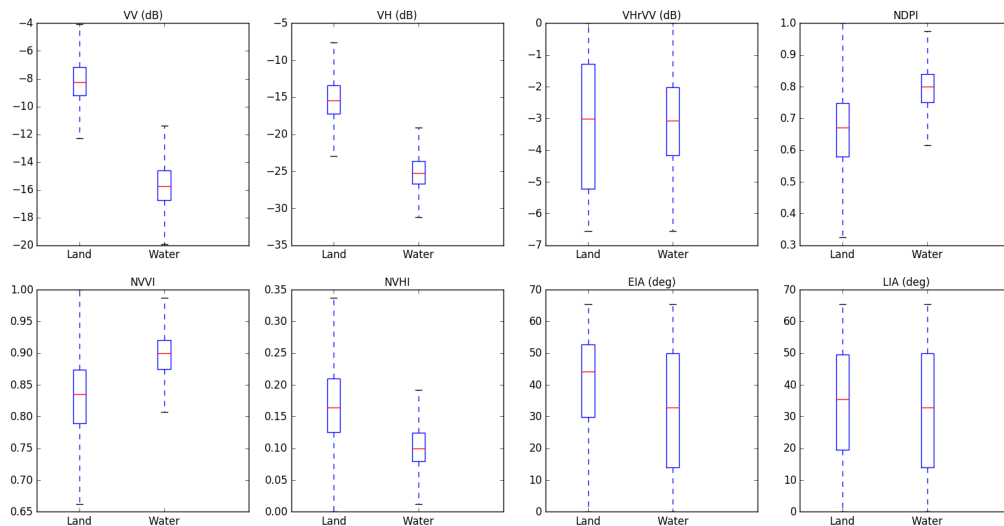


Figure 5. Box plot of polarized band, indices and geometry versus by land and water classes over Delmarva Peninsula. Red bar shows median and blue box represents first and third quartile. $VVrVH = VV/VH$, $NDPI = (VV - VH)/(VV + VH)$, $NVHI = VH/(VV + VH)$, $NVVI = (NVVI, VV/(VV + VH))$, EIA = ellipsoid incidence angle, and LIA = local incidence angle.

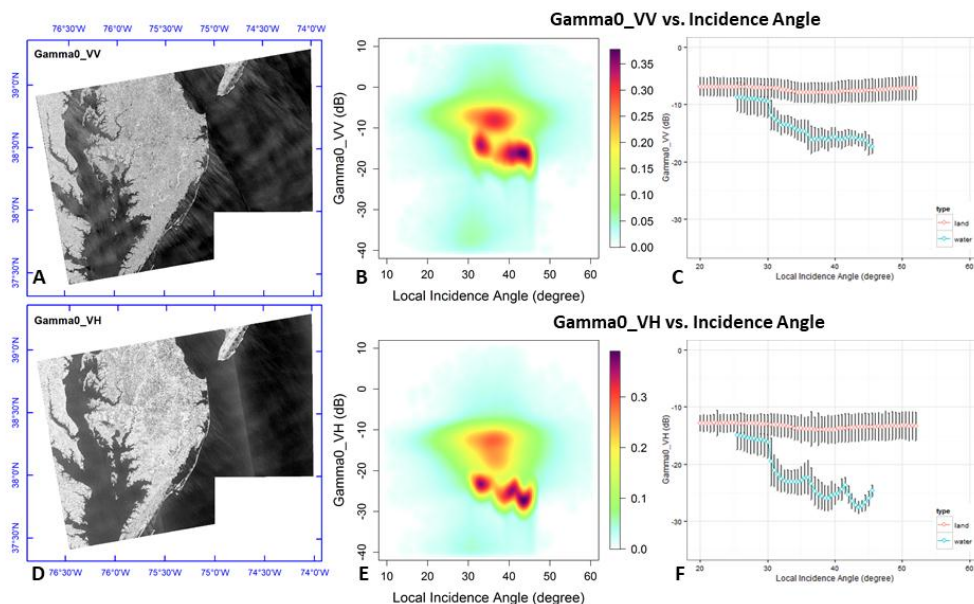


Figure 6. Γ_{VV} and Γ_{VH} (left column, (A,D)), density scatterplot (middle column, (B,E)), and binned scatterplot (right column, (C,F)) showing the separability between land and water classes defined by the SWBD in the Delmarva Peninsula. In the binned scatter plot, the backscatter coefficients (Γ_{VV} and Γ_{VH} in dB) are shown in cyan for water pixels and in red for land pixels. Grey bars represent 1 standard deviation.

3.3. Comparison of Classification Results

Classification results at Prairie Pothole Region and Delmarva sites are shown in Figure 7. The water/land classes derived from both SWBD and cDSWE prior masks followed reasonable patterns over large water bodies. At the Prairie Pothole Region site, the cDSWE-based results had fewer commission errors resulting from Bragg scattering from waves on open water and omission errors from the high probability water class compared to the results using SWBD (Figure 7A,C and subzoom). At the Delmarva site, increasing omissions of small and linear objects were observed from results using SWBD as a prior mask (Figure 7B,D and sub zoom).

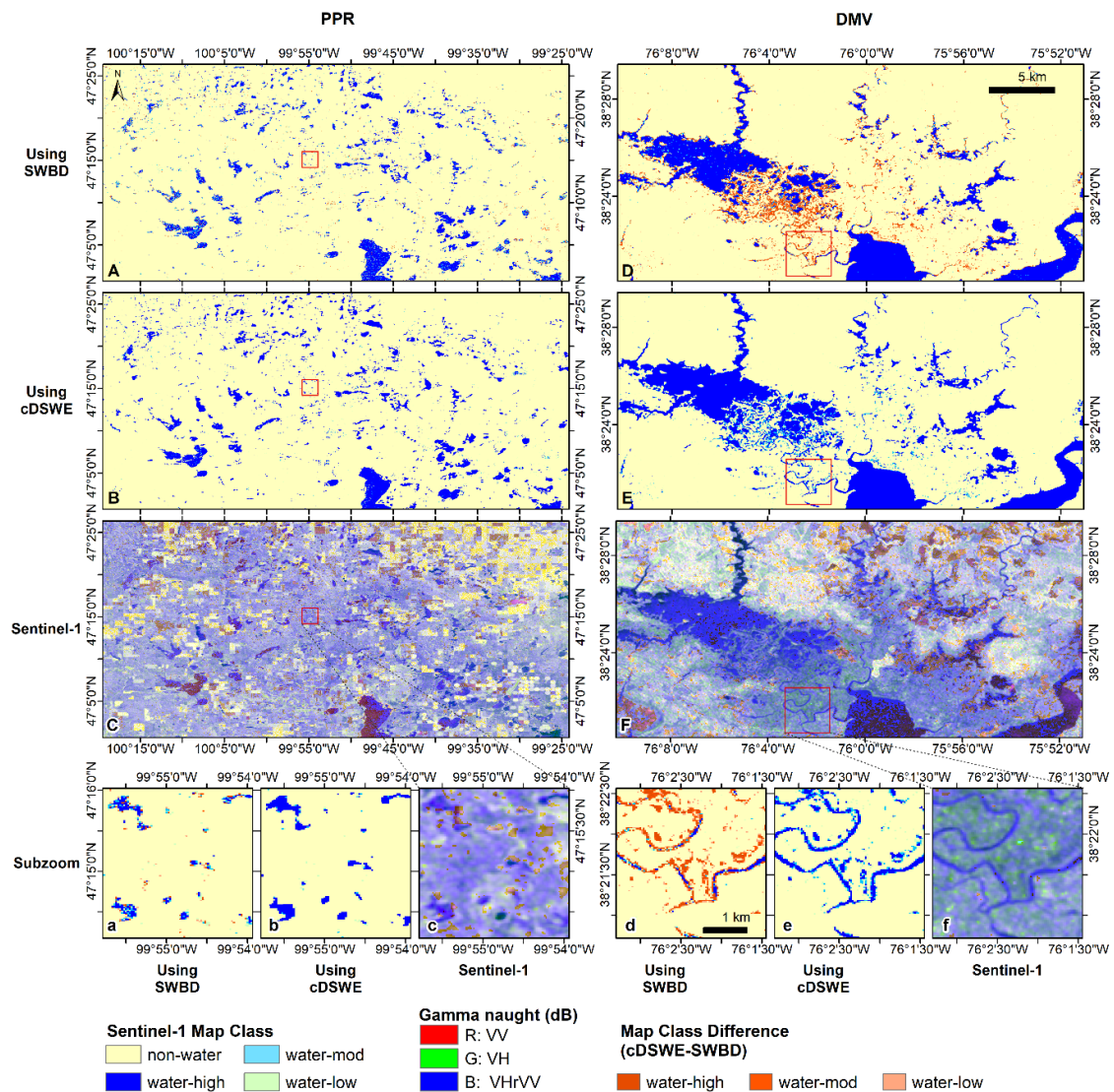


Figure 7. Random forest classification results over Prairie Pothole Region (PPR, left column, (A,B)) and Delmarva (DMV, right column, (D,E)) sites, using prior mask either from SWBD (top row) or composite DSWE (cDSWE) class probabilities (second row). The Sentinel-1 images (third row) were shown in false-color composited of Gamma naught (dB) (R: VV, G: VH, B: VVrVV), and were acquired on 10 August 2016 (E) and 9 July 2016 (F). The subzoom windows (bottom row) show small water bodies in PPR (left (a–c)) and linear streams (right (d–f)) missing from result using SWBD as prior mask. Difference in classification results between using SWBD and cDSWE were labeled in light to dark orange colors on the classification maps (A,B) and subzoom maps (a,d).

3.4. Validation and Accuracy Assessment

3.4.1. Comparison with DSWE Product

The classified Sentinel-1 maps and DSWE products from Landsat-8 images acquired within three days of the Sentinel-1 data are presented in Figure 8. Results indicate similar spatial patterns in both sites over water with high probability (“water-high”). For the Prairie Pothole Region site, the comparison between classified maps from Sentinel-1 and Landsat-8 DSWE indicated a closer pattern between the two results (Figure 8A,C). For the Delmarva site, the classification map derived from Sentinel-1 showed similar patterns as those from Landsat-8 derived DSWE over the high-probability water class (Figure 8B,D).

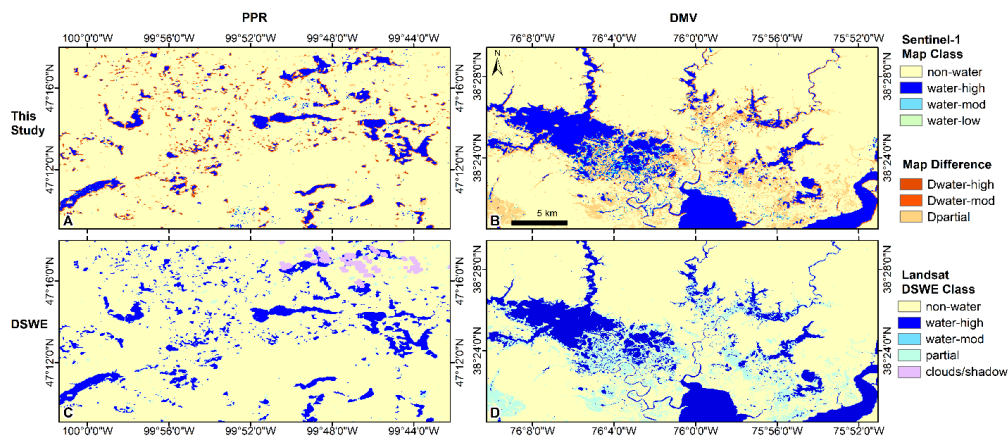


Figure 8. Comparison of classification maps derived from near-coincident Sentinel-1 (**upper row**) and Landsat-8 DSWE (**bottom row**), over the sites of Prairie Pothole Region (PPR, **left column**) and the Delmarva Peninsula (DMV, **right column**). The two Sentinel-1 classification maps were generated using cDSWE as prior mask from Sentinel-1 data collected on (B) 9 July 2016 and (D) 10 August 2016. The two DSWE products were generated from Landsat-8 data collected on (A) 11 July 2016 and (C) 11 August 2016. Difference in classification results between this study and DSWE are labeled in light to dark orange colors on the classification maps from this study (A,B).

3.4.2. Accuracy Assessment by High-Resolution Imagery

The classification results in 2016 from the Prairie Pothole Region site were validated using co-incident high-resolution imagery from NAIP. Accuracy assessments based on data collected on two dates (5 July 2016 and 10 August 2016) for classification derived using the SWBD and cDSWE datasets are presented in Table 3. Use of the cDSWE prior mask resulted in better accuracies (overall accuracy 82~93%, kappa 0.64~0.84) than use of the SWBD prior mask (overall accuracy 79~90%, kappa 0.54~0.77). Confusion matrix and accuracy estimates of the classification maps using the cDSWE prior mask are presented in Table 4.

Table 3. Comparison of overall accuracy, kappa coefficient, commission and omission errors between classification results using prior mask from SWBD and cDSWE over the Prairie Pothole Region site (PPR).

Site (Date)	Prior Mask	Overall Accuracy	Kappa Coefficient	Commission Error		Omission Error	
				Land	Water	Land	Water
A. PPR (4 July 2016)	SWBD	79%	0.54	29%	1%	1%	43%
	cDSWE	82%	0.64	26%	1%	1%	36%
B. PPR (9 August 2016)	SWBD	90%	0.77	8%	14%	6%	18%
	cDSWE	93%	0.84	4%	13%	6%	8%

Table 4. Confusion matrix and accuracy estimate (%) for classification maps over the Prairie Pothole Region site (PPR). (A) 5 July 2016 (UTC), overall accuracy = 82%, kappa coefficient = 0.64. (B) 10 August 2016 (UTC), overall accuracy = 93%, kappa coefficient= 0.84. Reference points were randomly sampled and manually interpreted from the high-resolution [1 m] NAIP images acquired on 5 July 2016 and 10 August 2016.

Site (Date)	Reference (from NAIP)					
	Class	Land	Water	Total	User's Accuracy	
A. PPR (5 July 2016)	Predicted	Land	150	52	202	74%
		Water	1	93	94	99%
		Total	151	145	296	
	Producer's accuracy		99%	64%		
					Overall Accuracy	82%
B. PPR (10 August 2016)	Predicted	Land	168	11	179	96%
		Water	7	76	83	87%
		Total	175	87	262	
	Producer's accuracy		94%	92%		
					Overall Accuracy	93%

3.5. Time-Series Classification Results

The time-series extent of surface water extracted using the Sentinel-1 data from April to September 2016 (Figure 9) revealed the dynamic nature of surface inundation in the Prairie Pothole Region site. The percentage of water summarized from the classification results for a subset in the PPR site (labelled 'A' in Figures 9 and 10) the response of surface water extent to increasing precipitation at local weather station. Specifically, higher percentages of surface water were observed on several dates (6 May, 30 May, 11 June, 17 July and 22 August), giving rises in precipitation (Figure 10).

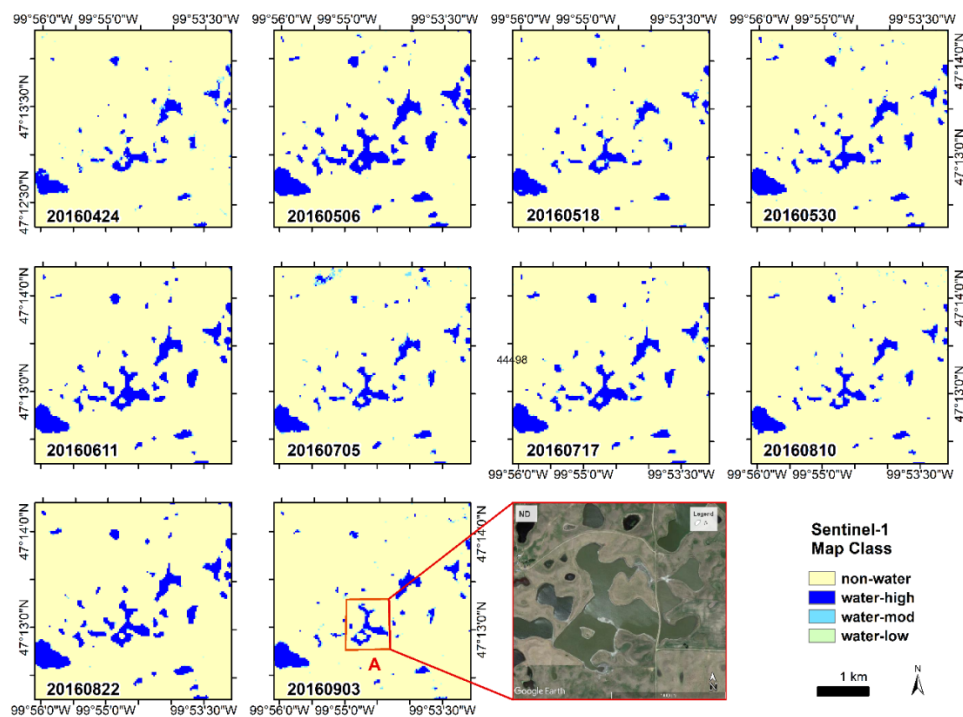


Figure 9. Classification results based on Sentinel-1 SAR data from April to September 2016, using cDSWE probabilities to derive training data for the Prairie Pothole Region site. The zoom-in window (A) was selected for illustrating change patterns of the surface water extent and weather data in Figure 10.

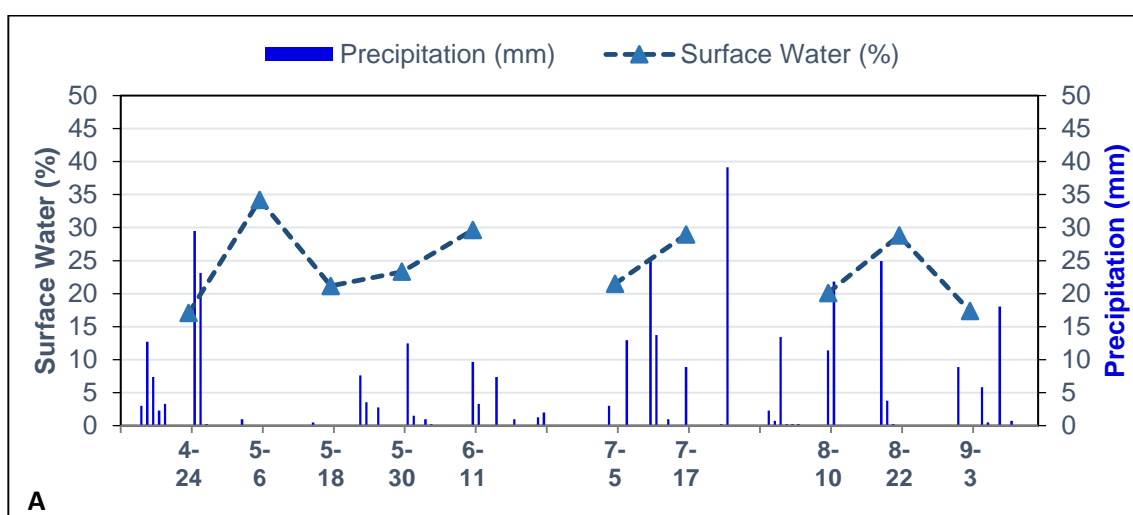


Figure 10. Time series of Sentinel-1 derived percentage of surface water extent (%) and precipitation (mm) for a subset in the Prairie Pothole Region site. The percentage of water was calculated from the time series of classification maps over the given inset in Figure 9. The daily precipitation data were collected by a nearby North Dakota Agricultural Weather Network (NDAWN) weather station in Robinson, ND [49].

4. Discussion

4.1. Significance of this Study

4.1.1. Automation of Algorithms

The developed fully automatic random forest classification tree approach to classify water and non-water over representative sites can be used to map the dynamics of surface waters at large geographical scales. Historically, preparing training datasets has often been a subjective and time-consuming step in this classification approach. In this paper, surface water extent was classified using training datasets automatically derived from prior class masks, thereby avoiding the time-consuming task of preparing training datasets. The preprocessing of Sentinel-1 data, preparation of prior masks (e.g., SWBD or cDSWE) and implementation of the classification were fully automated using open source software and packages (e.g., the SNAP toolbox gpt and several Python packages) in batch scripts. Only a few parameters (i.e., cDSWE thresholds, training sample size, random forest settings, and thresholds for class labeling) need to be stipulated by the user. However, the default values used in this study were found to be efficient in extracting surface water extent, and these parameter values were encoded within the batch scripts—allowing for full algorithm automation. Our algorithm computes water probabilities over an entire interferometric wide mode Sentinel-1 image (about 9500 by 7000 pixels) in less than 10 minutes (running on 15 parallel processors). Applying the same classification approach for Sentinel-1 images over different wetlandscapes, the automated algorithms were tested and validated the classification results through comparison with co-incident high-resolution imagery.

4.1.2. Improved Prior Masks for Classification

Separability of water and land classes in the prior masks is important for the classification model. Classification results using cDSWE were better than those using the SWBD at both study sites. This was expected for two reasons. First, SWBD is based on only one date (year 2000), whereas the 15-year composite DSWE probabilities account for seasonal/ephemeral inundation (Figure 4). Furthermore, the SWBD only maps water bodies that meet a minimum capture criteria of 600 m in length (i.e., about

4 × 4 30 m pixels) and 183 m in width (i.e., about 6 30 m pixels) for rivers and lakes, and 90 m in width (i.e., about 3 30 m pixel) for lake inlets/arms [44]. These features were delineated in the SWBD product regardless of whether they are dynamically inundated or not. On the other hand, the cDSWE-based training samples represent water and land classes in which any uncertain pixels (i.e., those variably classified as land or water throughout the 15-year time series) were excluded from training, reducing the commission errors in the water class (Figure 7). Second, the spatial resolutions of these two datasets were different. SWBD has a nominal spatial resolution of 90 m and includes only large rivers and lakes for inland water. By the minimum capture criteria, the small water bodies were excluded in SWBD. Being derived from Landsat imagery, the open water class cDSWE product has a 30 m spatial resolution and reveals sub-hectare inundation. With training samples for dynamic and small water bodies from cDSWE, the random forest models trained using cDSWE were, therefore, more sensitive to small water bodies (Figure 7).

4.1.3. Validation of Products

Validation of dynamic surface water mapping products can be very challenging and resource-intensive. Other remote sensing data offer a cost-effective alternative to field data for validation. Although validation using coincident high-resolution imagery was only implemented in the Prairie Pothole Region site, this approach could be extended when more coincident high-resolution images are available. Future validation of products from this algorithm at large geographical scales will rely on other high-resolution NAIP, Planet constellation [60], and commercial imagery. A series of factors may contribute to changes in surface water extent. Time-series classification results from the Prairie Pothole Region site provided insights in explaining response in surface water extent to environmental conditions such as precipitation in an inland wetlandscape.

4.2. Limitations and Potential Improvements

4.2.1. Omission from Inundated Vegetation

Omission errors were observed from inundated vegetation along rivers and lakes (Figure 8). This was also found in previous studies which concluded that fully polarimetric data (e.g., RASARSAT-2) are generally preferred for detecting flooded vegetation [23,31]. However, from the Sentinel-1 false-color backscatter composite (Figure 7), strong double bounce was observed from VH backscattering (in green color). The fact that these features were omitted is not unexpected, since the partial water class, defined as a pixel with mixed water and vegetation or soil reflectance signatures, was not included in the cDSWE prior masks due to limited area with probabilities above 95% (Figure 7). Future research will test whether compositing DSWE class probabilities on a seasonal basis would increase the number of high-probability partial-water pixels, allowing the inclusion of this class in the random forest model. In addition, for identifying inundated vegetation, future research could also test coherence and phase information from Sentinel-1, and decomposition information from experimental quad-polarization mode data from the RADARSAT-2. Additionally, the upcoming Radarsat Constellation Mission (RCM) [61] will provide operational compact polarimetry mode data, which has been recently demonstrated to be more effective than dual polarization approaches and nearly as effective as full polarimetric data at detecting inundated vegetation [62].

4.2.2. Resolution-Induced Omission Error

Omission errors were also noticed among small water bodies. In this study, we applied a commonly used filter (Lee Sigma) to reduce speckle-noise in radar images. Decreased spatial resolution was noticed after applying the filter, resulting in the omission of small water bodies in our classification maps. The lower producer's accuracy (64%) for water in the July 5 PPR results (Table 3) is mainly caused by this resolution-induced omission error. The July 5 PPR validation dataset covered a region (Figure 3 orange polygons in middle of the scene) that has more small water bodies than that from

the August 10 PPR validation region (Figure 3 red polygons in west and east of the scene). Recent studies suggest multi-temporal filters [63] and non-local speckle filters [64] could potentially reduce the speckle-noise while maintaining the original spatial resolution of the data.

4.2.3. Commission from Smooth Objects

Commission errors were observed from smooth objects like pavements and sandy surfaces. Recent studies have shown that the use of sand masks or road masks can reduce the overestimations introduced by sand in arid regions [54] or roads in urban areas [45]. Future research will test including external masks to reduce these commission errors.

5. Conclusions

In this study, fully automated algorithms were developed to derive water probability and classified maps of water and non-water over two distinct wetlandscapes using Sentinel-1 SAR data and historical Landsat data. Results indicated that using training data based on composite dynamic surface water extent products (i.e., cDSWE) together with random forests allows for the automated detection of surface water using Sentinel-1 SAR data. The classification maps followed reasonable patterns over the main water bodies, while increasing omission errors were observed from small, linear targets and inundated vegetation, and commission errors were noticed from sand and dark pavements. Importantly, the time-series results (Figure 9) revealed seasonal dynamics of inundation and provided insights in explaining the response in surface water extent to changes in precipitation. The fully automatic algorithms developed in this study can be implemented in an operational system to generate continental to global, long-term inundation records, including inundation-monitoring frameworks using satellite systems such as NASA and Indian Space Research Organization (ISRO) SAR mission (NISAR) and Canada's RADARSAT Constellation Mission (RCM) [61,65].

Author Contributions: W.H. processed the Sentinel-1 data, designed the experiments and wrote the manuscript. B.D. prepared the Landsat data and assisted in algorithm development. C.H., M.L. and J.W.J. conceived and designed the original study. I.F.C. and M.L.C reviewed and edited the first draft of the manuscript. All authors assisted in revising the manuscript.

Acknowledgments: The NASA Land-Cover and Land-Use Change (LCLUC) Program funded this research under contract NNX15AK66G. We would like to thank ESA's Sentinels Scientific Data Hub through Copernicus mission that provided the Sentinel-1 SAR data. We give special thanks to Google's Earth Engine which provided the archived Landsat data as well as computation capabilities. Particularly, we thank Jiaming Lu for preparing the NAIP data and Huiran Jin for variable discussions and comments that made the manuscript stronger.

Conflicts of Interest: The authors declare no conflict of interest. The findings and conclusions in this article are those of the authors and do not necessarily represent the views of the U.S. Fish and Wildlife Service. Any use of trade, firm, or product names is for descriptive purposes only and does not imply endorsement by the U.S. government.

References

1. Millennium Ecosystem Assessment Board. *Millennium Ecosystem Assessment Synthesis Report*; United Nation Environment Programme: New York, NY, USA, 2005.
2. Creed, I.F.; Lane, C.R.; Serran, J.N.; Alexander, L.C.; Basu, N.B.; Calhoun, A.J.; Christensen, J.R.; Cohen, M.J.; Craft, C.; D'Amico, E. Enhancing protection for vulnerable waters. *Nat. Geosci.* **2017**, *10*, 809. [[CrossRef](#)]
3. Krinner, G. Impact of lakes and wetlands on boreal climate. *J. Geophys. Res. Atmos.* **2003**, *108*. [[CrossRef](#)]
4. Shindell, D.T.; Faluvegi, G.; Bell, N.; Schmidt, G.A. An emissions-based view of climate forcing by methane and tropospheric ozone. *Geophys. Res. Lett.* **2005**, *32*. [[CrossRef](#)]
5. McDonough, O.T.; Lang, M.W.; Hosen, J.D.; Palmer, M.A. Surface hydrologic connectivity between delmarva bay wetlands and nearby streams along a gradient of agricultural alteration. *Wetlands* **2015**, *35*, 41–53. [[CrossRef](#)]
6. Lee, S.; Yeo, I.-Y.; Lang, M.; McCarty, G.; Sadeghi, A.; Sharifi, A.; Jin, H.; Liu, Y. Improving the catchment scale wetland modeling using remotely sensed data. *Environ. Model. Softw.* **2017**. [[CrossRef](#)]

7. Winter, T.C. Relation of streams, lakes, and wetlands to groundwater flow systems. *Hydrogeol. J.* **1999**, *7*, 28–45. [[CrossRef](#)]
8. Becker, M.W. Potential for satellite remote sensing of ground water. *Gr. Water* **2006**, *44*, 306–318. [[CrossRef](#)] [[PubMed](#)]
9. Wickham, J.D.; Stehman, S.V.; Fry, J.A.; Smith, J.H.; Homer, C.G. Thematic accuracy of the NLCD 2001 land cover for the conterminous united states. *Remote Sens. Environ.* **2010**, *114*, 1286–1296. [[CrossRef](#)]
10. Gong, P.; Wang, J.; Yu, L.; Zhao, Y.; Liang, L.; Niu, Z.; Huang, X.; Fu, H.; Liu, S.; et al. Finer resolution observation and monitoring of global land cover: First mapping results with Landsat TM and ETM+ data. *Int. J. Remote Sens.* **2013**, *34*, 2607–2654. [[CrossRef](#)]
11. Wulder, M.A.; Masek, J.G.; Cohen, W.B.; Loveland, T.R.; Woodcock, C.E. Opening the archive: How free data has enabled the science and monitoring promise of Landsat. *Remote Sens. Environ.* **2012**, *122*, 2–10. [[CrossRef](#)]
12. Drusch, M.; Del Bello, U.; Carlier, S.; Colin, O.; Fernandez, V.; Gascon, F.; Hoersch, B.; Isola, C.; Laberinti, P.; Martimort, P.; et al. Sentinel-2: ESA's optical high-resolution mission for GMES operational services. *Remote Sens. Environ.* **2012**, *120*, 25–36. [[CrossRef](#)]
13. Lang, M.; Bourgeau-Chavez, L.L.; Tiner, R.; Klemas, V. Chapter 5 Advances in Remotely Sensed Data and Techniques for Wetland Mapping and Monitoring. In *Remote Sensing of Wetlands: Applications and Advances*; CRC Press: Boca Raton, FL, USA, 2015.
14. Brisco, B. Mapping and monitoring surface water and wetlands with synthetic aperture radar. In *Remote Sensing of Wetlands: Applications and Advances*; Tiner, R., Lang, M., Klemas, V., Eds.; CRC Press: Boca Raton, FL, USA, 2015; pp. 119–136.
15. Kim, J.-W.; Lu, Z.; Jones, J.W.; Shum, C.K.; Lee, H.; Jia, Y. Monitoring everglades freshwater marsh water level using L-band synthetic aperture radar backscatter. *Remote Sens. Environ.* **2014**, *150*, 66–81. [[CrossRef](#)]
16. Santoro, M.; Wegmüller, U.; Lamarche, C.; Bontemps, S.; Defourny, P.; Arino, O. Strengths and weaknesses of multi-year Envisat ASAR backscatter measurements to map permanent open water bodies at global scale. *Remote Sens. Environ.* **2015**, *171*, 185–201. [[CrossRef](#)]
17. Cazals, C.; Rapinel, S.; Frison, P.-L.; Bonis, A.; Mercier, G.; Mallet, C.; Corgne, S.; Rudant, J.-P. Mapping and characterization of hydrological dynamics in a coastal marsh using high temporal resolution sentinel-1A images. *Remote Sens.* **2016**, *8*, 570. [[CrossRef](#)]
18. Bolanos, S.; Stiff, D.; Brisco, B.; Pietroniro, A. Operational surface water detection and monitoring using radarsat 2. *Remote Sens.* **2016**, *8*, 285. [[CrossRef](#)]
19. Martinis, S.; Kuenzer, C.; Wendleder, A.; Huth, J.; Twele, A.; Roth, A. Comparing four operational SAR-based water and flood detection approaches. *Int. J. Remote Sens.* **2015**, *36*, 3519–3543. [[CrossRef](#)]
20. Lang, M.W.; McCarty, G.W. Chapter 2 Remote Sensing Data for Regional Wetland Mapping in the United States: Trends and Future Prospects. In *Wetlands: Ecology, Conservation and Restoration*; Russo, R.E., Ed.; Nova Science Publishers. Inc.: Hauppauge, NY, USA, 2008.
21. Santoro, M.; Wegmüller, U. Multi-temporal synthetic aperture radar metrics applied to map open water bodies. *IEEE J. Sel. Top. Appl. Earth Obs. Remote Sens.* **2014**, *7*, 3225–3238. [[CrossRef](#)]
22. Westerhoff, R.; Kleuskens, M.; Winsemius, H.; Huizinga, H.; Brakenridge, G.; Bishop, C. Automated global water mapping based on wide-swath orbital synthetic-aperture radar. *Hydrol. Earth Syst. Sci.* **2013**, *17*, 651–663. [[CrossRef](#)]
23. Morandeira, N.; Grings, F.; Facchinetti, C.; Kandus, P. Mapping plant functional types in floodplain wetlands: An analysis of c-band polarimetric SAR data from Radarsat-2. *Remote Sens.* **2016**, *8*, 174. [[CrossRef](#)]
24. Clement, M.A.; Kilsby, C.G.; Moore, P. Multi-temporal synthetic aperture radar flood mapping using change detection. *J. Flood Risk Manag.* **2017**. [[CrossRef](#)]
25. Lang, M.W.; Townsend, P.A.; Kasischke, E.S. Influence of incidence angle on detecting flooded forests using C-HH synthetic aperture radar data. *Remote Sens. Environ.* **2008**, *112*, 3898–3907. [[CrossRef](#)]
26. Huang, W.; Sun, G.; Ni, W.; Zhang, Z.; Dubayah, R. Sensitivity of multi-source SAR backscatter to changes in forest aboveground biomass. *Remote Sens.* **2015**, *7*, 9587–9609. [[CrossRef](#)]
27. Smith, L.C.; Alsdorf, D.E. Control on sediment and organic carbon delivery to the arctic ocean revealed with space-borne synthetic aperture radar: Ob'river, Siberia. *Geology* **1998**, *26*, 395–398. [[CrossRef](#)]

28. Martinis, S.; Twele, A.; Voigt, S. Towards operational near real-time flood detection using a split-based automatic thresholding procedure on high resolution Terrasar-X data. *Nat. Hazards Earth Syst. Sci.* **2009**, *9*, 303–314. [[CrossRef](#)]
29. Matgen, P.; Hostache, R.; Schumann, G.; Pfister, L.; Hoffmann, L.; Savenije, H. Towards an automated SAR-based flood monitoring system: Lessons learned from two case studies. *Phys. Chem. Earth Parts A/B/C* **2011**, *36*, 241–252. [[CrossRef](#)]
30. Sun, F.; Sun, W.; Chen, J.; Gong, P. Comparison and improvement of methods for identifying waterbodies in remotely sensed imagery. *Int. J. Remote Sens.* **2012**, *33*, 6854–6875. [[CrossRef](#)]
31. Brisco, B.; Schmitt, A.; Murnaghan, K.; Kaya, S.; Roth, A. SAR polarimetric change detection for flooded vegetation. *Int. J. Digit. Earth* **2013**, *6*, 103–114. [[CrossRef](#)]
32. Berger, M.; Moreno, J.; Johannessen, J.A.; Levelt, P.F.; Hanssen, R.F. ESA's sentinel missions in support of earth system science. *Remote Sens. Environ.* **2012**, *120*, 84–90. [[CrossRef](#)]
33. Santoro, M.; Wegmuller, U.; Wiesmann, A.; Lamarche, C.; Bontemps, S.; Defourny, P.; Arino, O. Assessing Envisat ASAR and Sentinel-1 Multi-Temporal Observations to Map Open Water Bodies. In Proceedings of the 2015 IEEE 5th Asia-Pacific Conference on Synthetic Aperture Radar (APSAR), Singapore, 1–4 September 2015; pp. 614–619.
34. Feng, M.; Sexton, J.O.; Channan, S.; Townshend, J.R. A global, high-resolution (30-m) inland water body dataset for 2000: First results of a topographic-spectral classification algorithm. *Int. J. Digit. Earth* **2015**, 1–21. [[CrossRef](#)]
35. Klein, I.; Dietz, A.; Gessner, U.; Dech, S.; Kuenzer, C. Results of the global waterpack: A novel product to assess inland water body dynamics on a daily basis. *Remote Sens. Lett.* **2015**, *6*, 78–87. [[CrossRef](#)]
36. Zhang, H.K.; Roy, D.P. Using the 500 m MODIS land cover product to derive a consistent continental scale 30 m Landsat land cover classification. *Remote Sens. Environ.* **2017**, *197*, 15–34. [[CrossRef](#)]
37. Carroll, M.L.; Townshend, J.R.; DiMiceli, C.M.; Noojipady, P.; Sohlberg, R.A. A new global raster water mask at 250 m resolution. *Int. J. Digit. Earth* **2009**, *2*, 291–308. [[CrossRef](#)]
38. Pekel, J.-F.; Cottam, A.; Gorelick, N.; Belward, A.S. High-resolution mapping of global surface water and its long-term changes. *Nature* **2016**, *540*, 418. [[CrossRef](#)] [[PubMed](#)]
39. Gorelick, N.; Hancher, M.; Dixon, M.; Ilyushchenko, S.; Thau, D.; Moore, R. Google earth engine: Planetary-scale geospatial analysis for everyone. *Remote Sens. Environ.* **2017**, *202*, 18–27. [[CrossRef](#)]
40. Lang, M.; McDonough, O.; McCarty, G.; Oesterling, R.; Wilen, B. Enhanced detection of wetland-stream connectivity using lidar. *Wetlands* **2012**, *32*, 461–473. [[CrossRef](#)]
41. Huang, C.; Peng, Y.; Lang, M.; Yeo, I.-Y.; McCarty, G. Wetland inundation mapping and change monitoring using Landsat and airborne lidar data. *Remote Sens. Environ.* **2014**, *141*, 231–242. [[CrossRef](#)]
42. Torres, R.; Snoeij, P.; Geudtner, D.; Bibby, D.; Davidson, M.; Attema, E.; Potin, P.; Rommen, B.; Floury, N.; Brown, M.; et al. Gmes Sentinel-1 mission. *Remote Sens. Environ.* **2012**, *120*, 9–24. [[CrossRef](#)]
43. Copernicus Sentinel Data. Retrieved from ASF DAAC. Retrieved from ASF DAAC. Processed by ESA. 2016. Available online: <https://vertex.daac.asf.alaska.edu/> (accessed on 1 May 2017).
44. SWBD. Shuttle Radar Topography Mission Water Body Data Set. Digital Media 2005. Available online: https://dds.cr.usgs.gov/srtm/version2_1/ (accessed on 1 April 2016).
45. Jones, J. Efficient wetland surface water detection and monitoring via landsat: Comparison with in situ data from the everglades depth estimation network. *Remote Sens.* **2015**, *7*, 12503. [[CrossRef](#)]
46. Carroll, M.; Loboda, T. Multi-decadal surface water dynamics in North American tundra. *Remote Sens.* **2017**, *9*, 497. [[CrossRef](#)]
47. DeVries, B.; Huang, C.; Lang, M.; Jones, J.; Huang, W.; Creed, I. Automated quantification of surface water fraction in wetlands using optical Landsat and Sentinel-2 imagery. *Remote Sens.* **2017**, *9*. [[CrossRef](#)]
48. Vermote, E.; Justice, C.; Claverie, M.; Franch, B. Preliminary analysis of the performance of the Landsat 8/OLI land surface reflectance product. *Remote Sens. Environ.* **2016**, *185*, 46–56. [[CrossRef](#)]
49. NDAWN. North Dakota Agricultural Weather Network (NDAWN) Center. North Dakota State University, Ed. Fargo, North Dakota, 2016. Available online: <http://ndawn.ndsu.nodak.edu> (accessed on 12 March 2018).
50. Small, D. Flattening gamma: Radiometric terrain correction for SAR imagery. *IEEE Trans. Geosci. Remote Sens.* **2011**, *49*, 3081–3093. [[CrossRef](#)]

51. Lee, J.-S.; Wen, J.-H.; Ainsworth, T.L.; Chen, K.-S.; Chen, A.J. Improved sigma filter for speckle filtering of sar imagery. *IEEE Trans. Geosci. Remote Sens.* **2009**, *47*, 202–213.
52. Brisco, B.; Kapfer, M.; Hirose, T.; Tedford, B.; Liu, J. Evaluation of C-band polarization diversity and polarimetry for wetland mapping. *Can. J. Remote Sens.* **2011**, *37*, 82–92. [[CrossRef](#)]
53. Veloso, A.; Mermoz, S.; Bouvet, A.; Le Toan, T.; Planells, M.; Dejoux, J.-F.; Ceschia, E. Understanding the temporal behavior of crops using Sentinel-1 and Sentinel-2-like data for agricultural applications. *Remote Sens. Environ.* **2017**, *199*, 415–426. [[CrossRef](#)]
54. Mitchard, E.T.A.; Saatchi, S.S.; White, L.J.T.; Abernethy, K.A.; Jeffery, K.J.; Lewis, S.L.; Collins, M.; Lefsky, M.A.; Leal, M.E.; Woodhouse, I.H.; et al. Mapping tropical forest biomass with radar and spaceborne lidar in lopé national park, gabon: Overcoming problems of high biomass and persistent cloud. *Biogeosciences* **2012**, *9*, 179–191. [[CrossRef](#)]
55. García, M.; Saatchi, S.; Ustin, S.; Balzter, H. Modelling forest canopy height by integrating airborne lidar samples with satellite radar and multispectral imagery. *Int. J. Appl. Earth Obs. Geoinf.* **2018**, *66*, 159–173. [[CrossRef](#)]
56. McNairn, H.; Brisco, B. The application of C-band polarimetric SAR for agriculture: A review. *Can. J. Remote Sens.* **2004**, *30*, 525–542. [[CrossRef](#)]
57. Kim, Y.; Jackson, T.; Bindlish, R.; Lee, H.; Hong, S. Radar vegetation index for estimating the vegetation water content of rice and soybean. *IEEE Geosci. Remote Sens. Lett.* **2012**, *9*, 564–568.
58. Breiman, L. Random forests. *Mach. Learn.* **2001**, *45*, 5–32. [[CrossRef](#)]
59. Gabrielsen, C.G.; Murphy, M.A.; Evans, J.S. Using a multiscale, probabilistic approach to identify spatial-temporal wetland gradients. *Remote Sens. Environ.* **2016**, *184*, 522–538. [[CrossRef](#)]
60. McCabe, M.F.; Rodell, M.; Alsdorf, D.E.; Miralles, D.G.; Uijlenhoet, R.; Wagner, W.; Lucieer, A.; Houborg, R.; Verhoest, N.E.C.; Franz, T.E.; et al. The future of earth observation in hydrology. *Hydrol. Earth Syst. Sci.* **2017**, *21*, 3879–3914. [[CrossRef](#)]
61. Thompson, A.A. Overview of the radarsat constellation mission. *Can. J. Remote Sens.* **2015**, *41*, 401–407. [[CrossRef](#)]
62. Charbonneau, F.J.; Brisco, B.; Raney, R.K.; McNairn, H.; Liu, C.; Vachon, P.W.; Shang, J.; DeAbreu, R.; Champagne, C.; Merzouki, A.; et al. Compact polarimetry overview and applications assessment. *Can. J. Remote Sens.* **2010**, *36*, S298–S315. [[CrossRef](#)]
63. Quegan, S.; Le Toan, T.; Yu, J.J.; Ribbes, F.; Floury, N. Multitemporal ERS SAR analysis applied to forest mapping. *IEEE Trans. Geosci. Remote Sens.* **2000**, *38*, 741–753. [[CrossRef](#)]
64. Deledalle, C.-A.; Denis, L.; Tupin, F.; Reigber, A.; Jäger, M. Nl-SAR: A unified nonlocal framework for resolution-preserving (Pol)(In)SAR denoising. *IEEE Trans. Geosci. Remote Sens.* **2015**, *53*, 2021–2038. [[CrossRef](#)]
65. Rosen, P.A.; Kim, Y.; Kumar, R.; Misra, T.; Bhan, R.; Sagi, V.R. Global persistent SAR sampling with the NASA-ISRO SAR (NISAR) mission. In Proceedings of the 2017 IEEE Radar Conference (RadarConf), Seattle, WA, USA, 8–12 May 2017; pp. 0410–0414.

